PAPER

Uncertainties propagation and global sensitivity analysis of the frequency response function of piezoelectric energy harvesters

IOP Publishing Smart Materials and Structures
Smart Mater. Struct. 26 (2017) 065003 (14pp) https://doi.org/10.1088/1361-665X/aa6cf3

Uncertainties propagation and global sensitivity analysis of the frequency response function of piezoelectric energy harvesters

Rafael O Ruiz[1] **and Viviana Meruane**[2]

[1] Department of Civil Engineering, Universidad de Chile, Blanco Encalada 2002, Santiago, Chile
[2] Department of Mechanical Engineering, Universidad de Chile, Beauchef 851, Santiago, Chile

E-mail: rruizgarcia@ing.uchile.cl

Received 16 December 2016, revised 15 March 2017
Accepted for publication 12 April 2017
Published 2 May 2017

Abstract

The goal of this work is to describe a framework to propagate uncertainties in piezoelectric energy harvesters (PEHs). These uncertainties are related to the incomplete knowledge of the model parameters. The framework presented could be employed to conduct prior robust stochastic predictions. The prior analysis assumes a known probability density function for the uncertain variables and propagates the uncertainties to the output voltage. The framework is particularized to evaluate the behavior of the frequency response functions (FRFs) in PEHs, while its implementation is illustrated by the use of different unimorph and bimorph PEHs subjected to different scenarios: free of uncertainties, common uncertainties, and uncertainties as a product of imperfect clamping. The common variability associated with the PEH parameters are tabulated and reported. A global sensitivity analysis is conducted to identify the Sobol indices. Results indicate that the elastic modulus, density, and thickness of the piezoelectric layer are the most relevant parameters of the output variability. The importance of including the model parameter uncertainties in the estimation of the FRFs is revealed. In this sense, the present framework constitutes a powerful tool in the robust design and prediction of PEH performance.

Keywords: piezoelectric energy harvester, uncertainty propagation, Sobol indices

(Some figures may appear in colour only in the online journal)

1. Introduction

The dynamic description of piezoelectric energy harvesters (PEHs) has received significant attention in the last decade. The working principle of PEHs is based on their capability to convert dynamic deformations into electrical power when subjected to vibrations. The most common configuration consists of a cantilevered beam, which is composed of at least two layers of different materials; one that serves as structural support (typically a metal sheet), and the other that facilitates energy conversion (piezoelectric material). Figure 1 shows a schematic of these devices. Harvesters are classified according to the number of piezoelectric layers, i.e., unimorph and bimorph for configurations with one and two piezoelectric layers, respectively. These devices are characterized by large dimensions where the cantilevered beam length is in the order of 10^{-2} m [1]. However, smaller scale devices with piezoelectric layer thicknesses typically up to 10^{-4} m, generally microelectromechanical system (MEMS) harvesters, are also feasible owing to the adoption of specific deposition techniques [2].

For large scale PEHs (which are the focus of this work), different deterministic modeling techniques have been adopted to describe their electromechanical coupling effect. There are a wide range of different approaches, from simple models based on single degree of freedom dynamics [3–5], to more complex models base on Rayleigh–Ritz discrete formulations [6], finite element procedures [7], and adoption of modal

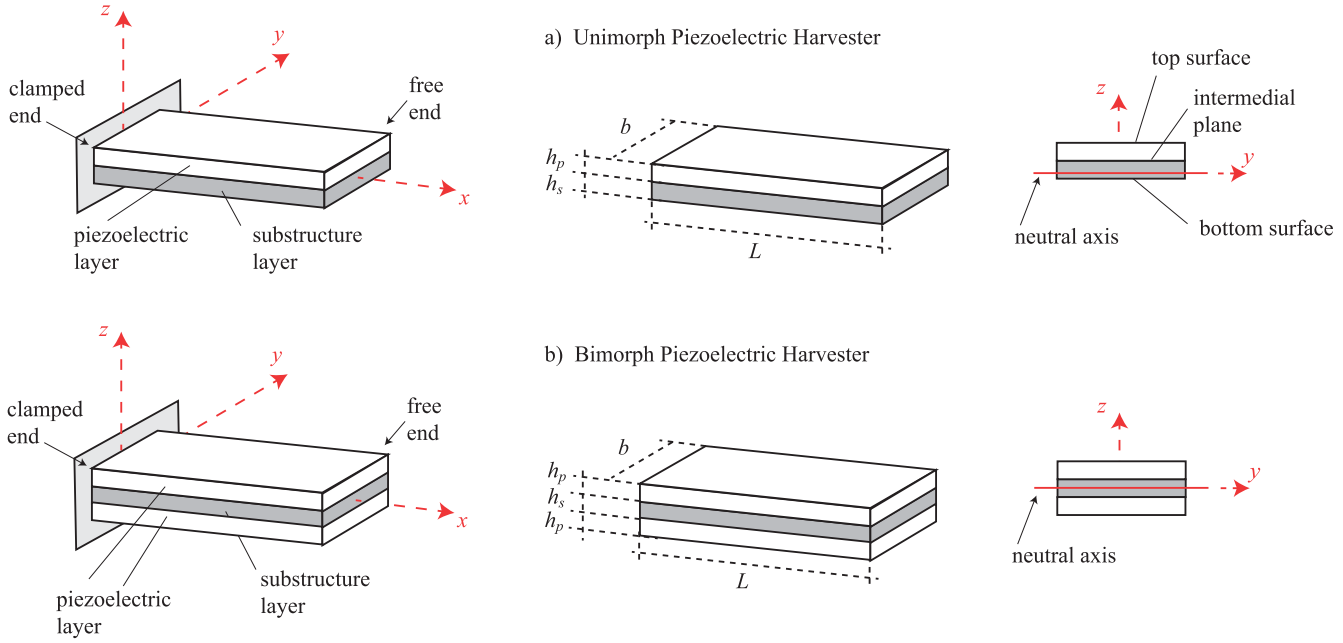

Figure 1. Geometric characteristics of unimorph (upper) and a bimorph (bottom) piezoelectric energy harvesters. (The tip mass and the external electric resistance are not showed.)

expansion techniques [8]. The latter is perhaps the most popular model since it takes into account a proper electro-mechanical effect and different beam vibration modes, and has a low computational cost since analytical solutions are presented [9]. In general, researchers have focused not only on the proposal of new and more sophisticated predictive models, but also on: (i) generation of configurations to collect energy from different environments, i.e., from aero-elastic structures [10, 11], fluid vortex and instabilities [12, 13], broad-band vibration sources [9, 14]; and (ii) design of efficient circuitry to rectify the output voltage to the required level [15]. Despite the great variety of research topics and contributions related to PEHs, there is a lack of studies regarding the adequate identification of the PEH dynamic; therefore, this topic is essential.

Deterministic models are widely-adopted to predict the input–output behavior of PEHs. However, perfect predictions are not expected since these devices contain uncertainties. The accuracy of the output estimation is mainly affected by the: (a) mathematical model used, (b) uncertainties in the mathematical model parameters, and (c) uncertainties related to the excitation. These uncertainties should be taken into account to generate robust and more plausible predictions. Nevertheless, limited attention has been paid to the uncertainty quantification and propagation related to the modeling of PEHs. Some efforts have been made in defining the excitation as a random variable [16] or prescribing probabilistic density functions to define the parametric dynamic characteristics of the harvester [17]. However, the analysis presented in [17] deals only with longitudinal excited harvesters and not with the conventional unimorph and bimorph harvesters subjected to transversal excitations. Additionally, the authors employed a simplified mechanical model, assuming a single degree of freedom, to propagate the uncertainties. In this sense, a more robust model is required, as well as general procedures that aid understanding the dynamic behavior of PEHs. The focus of this work is to describe a framework that not only allows the use of any well-known dynamic estimators in PEHs (traditional deterministic performance estimators), but takes into account the uncertainties in the model parameters. Specifically, the goal is to study the behavior of the frequency response functions of transversally-excited energy harvesters by the direct incorporation of uncertainties into the geometry and the electro-mechanical properties of the materials.

The framework consists of adopting a prior probability density function (PDF) for the uncertain variables. Then, the output estimation is established by the implementation of stochastic simulation techniques based on Monte Carlo methods. The PDF is chosen based on information available in the literature, which is also presented and organized here. Although these uncertainties quantification procedures are known, the main contribution of this research deals with: (1) adaption to the performance prediction of PEHs, (2) collection and presentation of the information available in the literature related to the variability of the model parameters, and (3) conduction of a variance-based sensitivity analysis to identify the most relevant model parameters. In this sense, the present framework constitutes a powerful tool in the robust design and prediction of PEH performance.

2. Piezoelectric energy harvester modeling

There are two procedures that have been used frequently by researchers: the analytical distributed parameter solution introduced by Erturk and Inman [5, 18] and the finite element plate model introduced by De Marqui Junior *et al* [7]. Since

the first procedure is well known by the scientific community, it is used in this research, in particular to study the effect of incomplete information related to the model parameters, e.g., uncertainties related to the piezoelectric constitutive equation, and incomplete geometry description. To clarify the notation used in this work, a summary of the analytical distributed parameters is presented next.

2.1. Analytical distributed parameter solution

This procedure allows estimation of the dynamic behavior of cantilevered PEHs under conventional configurations, including unimorph and bimorph, with and without tip masses. The cantilevered piezoelectric beam is modeled using the methodology introduced by Erturk and Inman [5, 18], which is based on a standard modal expansion method assuming an Euler–Bernoulli beam model. In particular, this methodology adopts some important assumptions such as: (i) the mechanical effect of the electrode layer is negligible since its thickness is significantly smaller than the substructure and the piezoelectric layers, (ii) the bonding between layers is perfect and does not influence the equivalent stiffness of the beam, and (iii) the thicknesses of the layers are invariant along the cantilever beam. These assumptions had been validated by Erturk and Inman through several experiments conducted using both unimorph and bimorph harvesters [1]. In this formulation, the relative displacement of any point of the beam with respect to its base is defined by $\delta = [\phi_1 \ \cdots \ \phi_M][\eta_1 \ \cdots \ \eta_M]^T = \boldsymbol{\phi}\boldsymbol{\eta}$, where η_i and ϕ_i denote the ith modal coordinate and the mass normalized eigenfunction (vibration mode), respectively. Furthermore, this procedure considers the electromechanical coupled effect, leading to a coupled system of differential equations of the following form:

$$\begin{aligned} &\ddot{\eta}_i + 2\zeta_i\omega_i\dot{\eta}_i + \omega_i^2\eta_i + \chi_i v = r_i\ddot{u}_g, \\ &\dot{v} + k_{\text{pzt}}v = \sum_{i=1}^{M}\varphi_i\dot{\eta}_i, \end{aligned} \tag{1}$$

where the first equation corresponds to the mechanical equation of motion with electrical coupling (cantilever beam with piezoelectric layers excited with an acceleration $\ddot{u}_g$ at its base), whereas the second equation corresponds to the electrical circuit equation with mechanical coupling. Note that in this particular case, the modal expansion is established by using M eigenfunctions. The damping ratio and the natural frequency of the 'ith' mode are defined by ζ_i and ω_i, respectively. The term χ_i takes into account the electric coupling for each vibrational mode, whereas the mechanical forcing function due to the inertial effect is defined as r_i. Additionally, v is defined as the output voltage; φ_i corresponds to the mechanical coupling term; and k_{pzt} is the parameter that contains the electrical characteristics of the harvester, i.e., the capacitance of the piezoelectric layer and the external electric resistance. For convenience, equation (1) is manipulated to express the problem in matrix form:

$$\begin{aligned} &\mathbf{I}\,\ddot{\boldsymbol{\eta}} + \mathbf{C}_{\text{eq}}\dot{\boldsymbol{\eta}} + \mathbf{K}_{\text{eq}}\boldsymbol{\eta} + \boldsymbol{\chi}v = \mathbf{r}\,\ddot{u}_g, \\ &\dot{v} + k_{\text{pzt}}v = \boldsymbol{\varphi}^T\dot{\boldsymbol{\eta}}. \end{aligned} \tag{2}$$

Here, $\mathbf{I} \in \mathbb{R}^{MxM}$ is the identity matrix; $\mathbf{C}_{\text{eq}} \in \mathbb{R}^{MxM}$ is a diagonal damping matrix containing the terms $2\zeta_i\omega_i$; $\mathbf{K}_{\text{eq}} \in \mathbb{R}^{MxM}$ is a diagonal matrix containing the squared natural frequencies ω_i^2; and $\boldsymbol{\chi}$, $\mathbf{r}$, $\boldsymbol{\eta}$, $\boldsymbol{\varphi} \in \mathbb{R}^{Mx1}$ are column vectors defined by χ_i, r_i, η_i, φ_i, respectively. Then, equation (2) can be used to obtain the respective transfer functions. In particular, the frequency response for the displacement of the beam and the output voltage are obtained assuming a base acceleration of $\ddot{u}_g = \ddot{U}_g e^{j\,\Omega\,t}$ (leading to a displacement $\delta = D\,e^{j\,\Omega\,t}$ and an output voltage $v = V\,e^{j\,\Omega\,t}$). Then, the following expressions are obtained:

$$\frac{D}{\ddot{U}_g} = \boldsymbol{\phi}\left[-\mathbf{I}\Omega^2 + j\Omega\mathbf{C}_{\text{eq}} + \mathbf{K}_{\text{eq}} + \frac{1}{j\Omega + k_{\text{pzt}}}\boldsymbol{\chi}\boldsymbol{\varphi}^T\right]^{-1}\mathbf{r}, \tag{3}$$

$$\begin{aligned} \frac{V}{\ddot{U}_g} = &\left(\frac{j\Omega}{j\Omega + k_{\text{pzt}}}\boldsymbol{\varphi}\right) \\ &\times\left[-\mathbf{I}\Omega^2 + j\Omega\mathbf{C}_{\text{eq}} + \mathbf{K}_{\text{eq}} + \frac{1}{j\Omega + k_{\text{pzt}}}\boldsymbol{\chi}\boldsymbol{\varphi}^T\right]^{-1}\mathbf{r}. \end{aligned} \tag{4}$$

To simplify the notation, we denote the mentioned transfer functions as $H_D = D/\ddot{U}_g$ and $H_V = V/\ddot{U}_g$. Ultimately, H_D and H_V can be related directly to the geometric, mechanical, and electrical characteristics of the PEH. These relationships are explicitly identified for unimorph and bimorph harvesters in [5, 18], respectively.

2.2. Uncertainties in the electromechanical and geometric characteristics of PEH

In general, the precision in the estimation of the frequency response functions H_D and H_V depends on the information available (usually incomplete) related to the geometry and the electromechanical properties of the harvester. However, the issue is not related to the lack of information itself, rather its impact on the predicted response. Specifically, the goal is to identify the dominant parameter or a group of parameters in terms of precision in the predictive model. The lack of information can be assumed as an uncertainty that can be modeled by a probabilistic distribution associated with the geometry and electromechanical parameters of the harvester. Then, it is possible to implement a procedure to propagate this uncertainty and identify the parameters that have a significant impact on the response. However, the uncertainties associated with PEH parameters should be discussed first. In this section, an overview of the most relevant uncertainties in PEH is presented.

For convenience, the characteristics of the harvester are divided into three groups: geometric specifications, mechanical properties of the substructure layer, and electrical/mechanical properties of the piezoelectric layer. The geometric specifications of the harvester contain the information

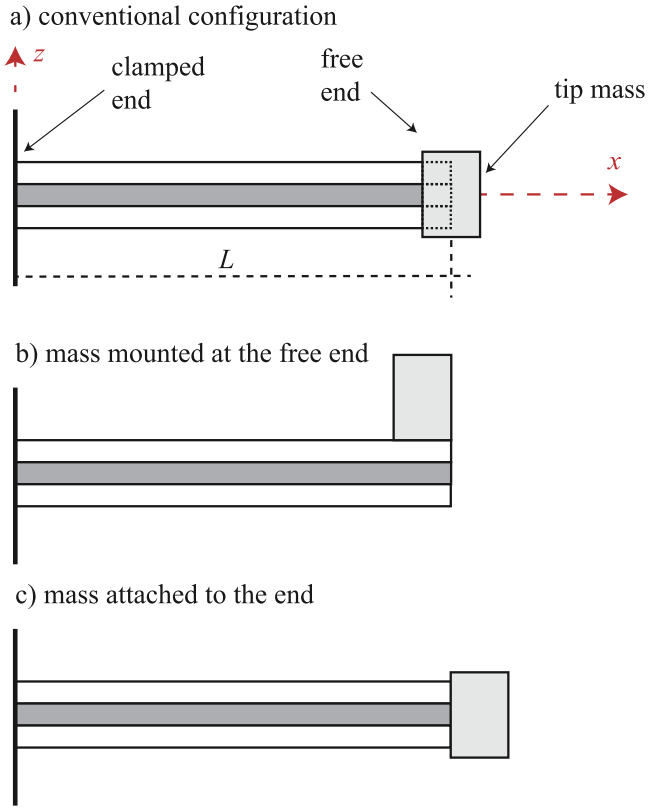

Figure 2. Different mounting strategies for the tip mass in cantilevered PEH: (a) point mass model, (b) tip mass mounted on the beam, and (c) tip mass attached to the end of the beam.

related to the beam length L and width b, together with the thickness of the piezoelectric and the substructure layers, h_p and h_s, respectively (figure 1). Manufacturing tolerances are not typically associated with these values. However, some manufacturers report variations up to 25% in the beam thickness and up to 7% for the beam length and width. For instance, table 1 presents manufacturing tolerances associated with the geometrical characteristics of the harvester. Note that the variation expected for the thickness is considerably greater than the expected values for the remaining geometrical parameters. In fact, the smaller the dimension, the more difficult it is to maintain precision in the fabrication process.

It is important to mention that the incorporation of the tip mass in the cantilever beam and the system used to attach the beam to its base introduce additional uncertainties. Note that the common approach to introduce the tip mass in the analysis is to assume a point mass [18, 22], which is valid for masses with small dimensions where the rotational inertia can be neglected. This assumption corresponds to the case in which the whole mass is located at the free end of the beam (figure 2(a)). However, in practical applications, the tip mass may be mounted at the free end of the beam (figure 2(b)) or simply attached to the end (figure 2(c)). In both cases, the effective length L of the beam is affected, obtaining a worst-case scenario variation of L equal to half of the tip mass length. On the other hand, the clamping quality also affects the effective length L, since an inadequate clamping system (non-zero curvature at $x = 0$) can be interpreted as an increment in the beam length.

The second group of variables with uncertainties contains the information related to the mechanical properties associated with the substructure layer, i.e., Young's modulus Y_s and the density ρ_s. It is important to note that there is not a common adoption of the material used in the substructure layer; nevertheless typical applications use iron–nickel alloys, bronze, and copper [19], as well as brass [5, 7, 19], aluminum [22], and silicon (usually employed in MEMS harvesters) [23], among others. In general, the Young's modulus values for these metals are of the order of 10^{10}–10^{11} Pa. However, the specific value for each material depends on its composition and its mechanical and thermal history [24]. Furthermore, Young's modulus is typically used as a deterministic value (commonly found in general material property tables), when in reality it represents only the expected value for a specific material. In particular, for the materials mentioned above, the variations in the Young's modulus are $\pm 10\%$ of their nominal values [25, 26]. Similar variations are also reported for the nominal density values [26].

The third group of uncertain variables is primarily related to the electrical/mechanical characteristics of the piezoelectric layer, more specifically, to the elastic modulus of the piezoelectric layer Y_p and its density ρ_p, the permittivity at constant strain ε_{33}^s, and the piezoelectric coupling coefficient e_{31}. The PEH employed in this work corresponds to a conventional poled harvester (d_{31} mode); thus, a fully covered electrode is used. However, the methodology to propagate the uncertainties could be extended easily to MEMS harvesters (where, typically, the electrode is interdigitated) by using an adequate model predictor. Here, additional comments regarding the constitutive relation of the piezoelectric material are required. The constitutive relation for a cantilevered piezoelectric beam is usually expressed as the following:

$$\begin{aligned} T_1 &= Y_p S_1 - e_{31} E_3, \\ D_3 &= e_{31} S_1 + \varepsilon_{33}^s E_3, \end{aligned} \tag{5}$$

where T_1, S_1, E_3, and D_3 correspond to the normal stress, normal strain, electric field, and electric displacement, respectively. Here, subscripts 1 and 3 denote the principal directions in x and z, respectively. Based on the plane stress assumption for an isotropic thin beam, some important relations are identified. In particular, the elastic modulus Y_p, the piezoelectric coupling coefficient e_{31}, and the permittivity at constant strain ε_{33}^s, can be expressed as functions of the elastic compliance at constant electric field s_{11}^E, piezoelectric strain constant d_{31}, and permittivity at constant stress ε_{33}^T. These relations are given by the following:

$$Y_p = \frac{1}{s_{11}^E}; \quad e_{31} = \frac{d_{31}}{s_{11}^E}; \quad \varepsilon_{33}^s = \varepsilon_{33}^T - \frac{d_{31}^2}{s_{11}^E}. \tag{6}$$

The latter equation is particularly useful since s_{11}^E, d_{31}, and ε_{33}^T are widely used to define the constitutive equation for piezoelectric materials, e.g., the piezoelectric material properties presented in [1, 20, 27, 28]. Although the electromechanical characteristics of piezoelectric materials are

Table 1. Tolerances for different geometries of PEH.

Nominal values	Tolerances	Nominal values	Tolerances
$b < 10$ mm	±7.0% [19]	h_p, h_s close to 0.2 mm	±25% [20]
L, $b > 10$ mm	±3.0% [20]	h_p, h_s close to 0.2 mm	±12% [21]
$b > 10$ mm	±3.0% [19]	h_p, $h_s < 0.3$ mm	±10% [19]
L, $b > 13$ mm	±2.0% [21]	h_p, h_s close to 0.5 mm	±4% [22]
$L < 50$ mm	±2.5% [19]	h_p, h_s close to 1 mm	±5% [20]
$L > 50$ mm	±1.0% [19]	h_p, $h_s > 5$ mm	±1% [21]

commonly reported by manufacturers, typically limited information regarding their tolerances is reported. For example, a tolerance of ±20% is reported for all electro-mechanical characteristics in [20, 29]. To the best of our knowledge, no further specific information is available in the literature. Therefore, we decided to use the mentioned tolerance value (±20% for all electro–mechanical properties) in all the analyses conducted in this work. The final characteristic of the harvester that should be mentioned is the external electric resistance R. This resistance represents the electronic power load that the harvester is required to move. This load and the corresponding precision in its estimation may change depending on the application.

Finally, the characteristics of the harvesters are grouped as follows:

$$\begin{aligned}\boldsymbol{\theta}_g &= \begin{bmatrix} L & b & h_s & h_p \end{bmatrix},\\ \boldsymbol{\theta}_s &= \begin{bmatrix} Y_s & \rho_s & M_t \end{bmatrix},\\ \boldsymbol{\theta}_p &= \begin{bmatrix} Y_p & \rho_p & d_{31} & \varepsilon_{33}^T & R \end{bmatrix},\end{aligned} \tag{7}$$

where $\boldsymbol{\theta}_g$, $\boldsymbol{\theta}_s$, and $\boldsymbol{\theta}_p$ correspond to vectors with geometrical characteristics, mechanical properties of the substructure layer, and electromechanical properties of the piezoelectric layer, respectively. For the sake of simplicity, these characteristics are grouped such that $\boldsymbol{\theta} = \begin{bmatrix} \boldsymbol{\theta}_g & \boldsymbol{\theta}_s & \boldsymbol{\theta}_p \end{bmatrix}$, where $\boldsymbol{\theta}$ is defined as the model parameter vector. Since the parameters of the harvester present a level of variation, it is assumed that the model parameter vector lies in space (defined by the individual variability) instead of adopting a deterministic value. Based on this, section 3 presents a procedure to propagate these uncertainties and quantify their impacts on the dynamic response of the harvester.

3. Robust stochastic prediction

Some concepts related to stochastic prediction in dynamical systems are revisited in this section. First, a general approach is presented and then the procedure is particularized to propagate uncertainties in PEHs.

3.1. Predictive analysis

Suppose that the deterministic model defines the relationship $\mathbf{H}(\boldsymbol{\theta})$, where $\boldsymbol{\theta} \in \mathbb{R}^{Np}$ corresponds to the model parameters vector. An additive prediction error $\mathbf{e}$ is usually included here such that the real system output $\mathbf{h} \in \mathbb{R}^{No}$ is defined by $\mathbf{h} = \mathbf{H}(\boldsymbol{\theta}) + \mathbf{e}$. A common practice is to assume a Gaussian error with zero mean (imposing an unbiased prediction) and covariance matrix $\boldsymbol{\Sigma}$; this condition forces $\mathbf{h}$ to follow a Gaussian distribution with mean $\mathbf{H}(\boldsymbol{\theta})$ and covariance matrix $\boldsymbol{\Sigma}$ (further details provided in [30]):

$$p(\mathbf{h}|\ \boldsymbol{\theta}) = \frac{1}{\sqrt{|\boldsymbol{\Sigma}|}\,(2\pi)^{No/2}} \exp\left[-\frac{1}{2}(\mathbf{h} - \mathbf{H}(\boldsymbol{\theta}))^T \times \boldsymbol{\Sigma}^{-1}(\mathbf{h} - \mathbf{H}(\boldsymbol{\theta}))\right]. \tag{8}$$

Here, $p(\mathbf{h}|\ \boldsymbol{\theta})$ represents the PDF of the real output $\mathbf{h}$ given the model parameter $\boldsymbol{\theta}$. Since the prediction error assumed here is an additive error which follows a Gaussian distribution with zero mean, the expected value of $\mathbf{h}$ and $\mathbf{H}$ are equal, see equation (9).

$$E[\mathbf{h}] = E[\mathbf{H} + \mathbf{e}] = E[\mathbf{H}] + E[\mathbf{e}] = E[\mathbf{H}]. \tag{9}$$

Note that if the model parameter $\boldsymbol{\theta}$ is known, the expected value of the real system is simply the value $\mathbf{H}$ at the interest point $\boldsymbol{\theta}$, holding the following relation:

$$E[\mathbf{h}\ |\boldsymbol{\theta}] = \int \mathbf{h}\, p(\mathbf{h}\ |\boldsymbol{\theta}) \mathrm{d}\mathbf{h} = E[\mathbf{H}\ |\boldsymbol{\theta}] = \mathbf{H}(\boldsymbol{\theta}). \tag{10}$$

Now, it is possible to propagate uncertainties related to the model parameters. To achieve this, the model parameters should be described by a PDF, which in this case is denoted as $p(\boldsymbol{\theta})$. Then, equation (10) is extended to include $p(\boldsymbol{\theta})$ as follows:

$$E[\mathbf{h}] = \int\int \mathbf{h}\, p(\mathbf{h}\ |\boldsymbol{\theta}) p(\boldsymbol{\theta}) \mathrm{d}\mathbf{h}\mathrm{d}\boldsymbol{\theta}. \tag{11}$$

This equation defines the expected value of the real output $E[\mathbf{h}]$, however, this concept could be extended to define the expected value of any other performance function $\mathbf{f}(\mathbf{h})$ such that

$$E[\mathbf{f}(\mathbf{h})] = \int\int \mathbf{f}(\mathbf{h}) p(\mathbf{h}\ |\boldsymbol{\theta}) p(\boldsymbol{\theta}) \mathrm{d}\mathbf{h}\mathrm{d}\boldsymbol{\theta}. \tag{12}$$

Furthermore, if the goal is to work with the expected value of the real output, then it is possible to simplify equation (11) using the results determined from equation (10), leading to

$$E[\mathbf{h}] = \int \mathbf{H}(\boldsymbol{\theta}) p(\boldsymbol{\theta}) \mathrm{d}\boldsymbol{\theta}. \tag{13}$$

Note that the dimension of the integral presented in equation (13) corresponds to the dimension of $\boldsymbol{\theta}$. Analytical calculation of these integrals is impractical (apart from special and simple cases) and calculation through numerical integration is inefficient for dimensions $\geqslant 3$ (note that for N evaluations, the approximation error for standard numerical

integration is $O(N^{-1/n})$, where n is the integral dimension). As a consequence, the probabilistic integral is commonly solved via stochastic-simulations, corresponding to a broad class of computational methods that are sampling-based, e.g., Monte Carlo family methods [31]. Next, an overview of the direct Monte Carlo method is presented.

3.2. Direct Monte Carlo simulation

This method numerically approximates an integral of the form presented in equation (13). The first step of this method corresponds to the generation of samples that follow $p(\boldsymbol{\theta})$. Let us assume that it is easy to generate these samples, i.e., $p(\boldsymbol{\theta})$ corresponding to a well-known distribution: normal, Gaussian, weibull etc. The first step consists of generating K samples of $\boldsymbol{\theta}$, forming a set of data denoted $\{\boldsymbol{\theta}^j, j = 1,..., K\}$, such that the total set follows the distribution $p(\boldsymbol{\theta})$. The second step consists of estimating the output of the system using each $\boldsymbol{\theta}^j$ obtained previously, generating a set of data denoted $\{H(\boldsymbol{\theta}^j), j = 1,..., K\}$. Finally, based on the central limit theorem, the Monte Carlo method estimates the probabilistic integral (equation (13)) as:

$$\hat{\mathbf{h}} = \frac{1}{K}\sum_{j=1}^{K}\mathbf{H}(\boldsymbol{\theta}^j). \tag{14}$$

Here, $\hat{\mathbf{h}}$ is the approximation of $E[\mathbf{h}]$ made using the Monte Carlo method, and it simply corresponds to the mean value of the output dataset. Based on this, the concern that arises is the number of samples that should be computed, in other words, the determination of K. To address this, let us assume that the complete process (sampling, output identification, and averaging) is repeated multiple times. For instance, if the dataset $\{\boldsymbol{\theta}^j, j = 1,..., K\}$ is generated m times, then it is expected to have m values of $\hat{\mathbf{h}}$. All of these m values of $\hat{\mathbf{h}}$ will closely approximate $E[\mathbf{h}]$ (which is the theoretical mean), and thus, the variance could be used as a precision indicator. The smaller the variance, the better the approximation. Fortunately, it is possible to estimate this variance using only one set of data rather than m sets. A more convenient expression to define the precision is through the coefficient of variation (c.o.v). Note that $\mathbf{H}$ is not necessary a scalar; it contains as many entries as the system output, such that $\mathbf{H} = \begin{bmatrix} H_1 & \cdots & H_i & \cdots & H_{No} \end{bmatrix}$. Finally, the c.o.v of the estimator for the ith output has the following expression:

$$\delta_{\mathrm{MC}_i} = \frac{1}{\sqrt{K}} \frac{\sqrt{\frac{1}{K}\sum_{j=1}^{K}(H_i(\boldsymbol{\theta}^j))^2 - \left(\frac{1}{K}\sum_{j=1}^{K}H_i(\boldsymbol{\theta}^j)\right)^2}}{\frac{1}{K}\sum_{j=1}^{K}H_i(\boldsymbol{\theta}^j)}. \tag{15}$$

Here, it is observed that δ_{MC} approaches zero if K approaches infinity, indicating that the direct Monte Carlo method is an unbiased and convergent estimator. Additionally, note that, through equation (15), it possible to estimate the number of samples required to guarantee a specific precision.

3.3. Sensitivity analysis

In probabilistic studies, there is another important analysis that can be performed, namely the variance decomposition or analysis of variance. This analysis relies on the decomposition of the output variance into individual contributions attributed to each model parameter and their interactions. Here, the goal is to identify the impact of the model parameters on the output variance. In the case of the energy harvester, the analysis of variance allows classification of the parameters or groups associated with the geometric characteristics, mechanical, or electrical properties that strongly dominate the output voltage and the beam tip displacement, and which have limited or no impact. A common procedure to quantify the sensibility of the model parameters is the estimation of the Sobol indices [32, 33]. Some important definitions regarding this analysis are presented next.

Let $H_i(\boldsymbol{\theta})$ denote the ith output of the system, which depends on the model parameter vector $\boldsymbol{\theta}$. Sobol indices are usually expressed for model parameters $\boldsymbol{\theta}$ that are independent and uniformly distributed from zero to one [32, 33]. However, it is possible to extend the Sobol indices concept for other types of distribution [34], such that the model parameter vector $\boldsymbol{\theta} \in \Theta$ could be defined by an arbitrary PDF $p(\boldsymbol{\theta})$. Here, Θ corresponds to the space of possible values for $\boldsymbol{\theta}$. Adopting a random PDF for $\boldsymbol{\theta}$, the mean and the variance of the ith output are given, respectively, by

$$\mu_i = \int_{\Theta} H_i(\boldsymbol{\theta})p(\boldsymbol{\theta})\mathrm{d}\boldsymbol{\theta}, \tag{16}$$

$$V_i = \int_{\Theta} H_i(\boldsymbol{\theta})^2 p(\boldsymbol{\theta})\mathrm{d}\boldsymbol{\theta} - \mu_i^2. \tag{17}$$

Now, let $\boldsymbol{\theta}_n \in \Theta_n$ be the nth independent model parameter and $\boldsymbol{\theta}_{\sim n} \in \Theta_{\sim n}$ the remaining model parameter vector (containing all parameters in $\boldsymbol{\theta}$ except $\boldsymbol{\theta}_n$). This notation is extended to describe high-order interactions. Then, multiple subscripts are used to group independent variables, for example, $\boldsymbol{\theta}_{nm} \in \Theta_{nm}$ is a vector composed of $\boldsymbol{\theta}_n$ and $\boldsymbol{\theta}_m$, whereas $\boldsymbol{\theta}_{\sim nm} \in \Theta_{\sim nm}$ is a vector composed of $\boldsymbol{\theta}$, excluding $\boldsymbol{\theta}_n$ and $\boldsymbol{\theta}_m$. It is important to note that either $\boldsymbol{\theta}_n$ and $\boldsymbol{\theta}_m$ could be defined not only by one parameter, but by a group of them; the only restriction is that the grouped parameters in $\boldsymbol{\theta}_n$ should be independent of $\boldsymbol{\theta}_{\sim n}$ and the group of $\boldsymbol{\theta}_{nm}$ should be independent of $\boldsymbol{\theta}_{\sim nm}$. Additionally, let us define V_n and V_{nm} as the variance contribution of $\boldsymbol{\theta}_n$ and $\boldsymbol{\theta}_{nm}$ over the total output variance, respectively. This variance decomposition leads to:

$$V_i = \sum_{n=1}^{N} V_n + \sum_{n=1}^{N-1}\sum_{m=1}^{N} V_{nm} + \cdots. \tag{18}$$

Here, N denotes the total number of independent model parameters, where the first and second order variances V_n and V_{nm} can be obtained by solving the following integrals:

$$V_n = \int_{\Theta_n}\left[\int_{\Theta_{\sim n}} H_i(\boldsymbol{\theta})p(\boldsymbol{\theta}_{\sim n})\mathrm{d}\boldsymbol{\theta}_{\sim n}\right]^2 p(\boldsymbol{\theta}_n)\mathrm{d}\boldsymbol{\theta}_n, \tag{19}$$

Table 2. Nominal characteristic of the harvesters studied; three different geometries are presented, where configurations A and B are unimorphs and configuration C is a bimorph.

	Configuration A	Configuration B	Configuration C
L	97.66 mm	100 mm	50.8 mm
b	73.41 mm	20 mm	31.8 mm
h_p	0.26 mm	0.4 mm	0.26 mm
h_s	0.28 mm	0.5 mm	0.14 mm
ρ_s	8140 kg m^{-3}	7165 kg m^{-3}	9000 kg m^{-3}
Y_s	100 GPa	100 GPa	105 GPa
ζ	0.01 (for all modes)	0.01 (for all modes)	0.01 (for all modes)

$$V_{nm} = \int_{\Theta_{nm}} \left[\int_{\Theta_{\sim nm}} H_i(\boldsymbol{\theta}) p(\boldsymbol{\theta}_{\sim nm}) \mathrm{d}\boldsymbol{\theta}_{\sim nm} \right]^2 p(\boldsymbol{\theta}_{nm}) \mathrm{d}\boldsymbol{\theta}_{nm} - V_n - V_m - \mu_i. \tag{20}$$

Finally, the Sobol indices are defined through equation (21), where S_n corresponds to the first-order index for $\boldsymbol{\theta}_n$ and S_{nm} corresponds to the second-order index for interactions between $\boldsymbol{\theta}_n$ and $\boldsymbol{\theta}_m$. For more detailed information, please refer to [35].

$$S_n = \frac{V_n}{V_i}; \quad S_{nm} = \frac{V_{nm}}{V_i}. \tag{21}$$

To identify the Sobol indices, the multidimensional probabilistic integrals presented in equations (19) and (20) must be solved. The common approach to solve these integrals is through the implementation of Monte Carlo simulations, as described in [33]. This procedure entails significant computational cost, i.e., for K samples, the identification of each S_n requires NK evaluations of the system, whereas the estimation of each S_{nm} requires $N(N-1)/2$ additional evaluations. However, we decided to employ a Monte Carlo simulation since the output of the energy harvester, obtained via analytical solution, does not represent a significant computational burden. For the sake of brevity, the numerical scheme to solve equations (19) and (20) is not presented here; nevertheless full details of this procedure can be found in [33].

4. Uncertainty propagation in PEHs

The schemes described previously to perform a robust prediction and to conduct a sensitivity analysis are applied to different configurations of PEH, in particular, to unimorph and bimorph harvesters.

4.1. Properties of PEH

Two unimorph and one bimorph harvesters with different geometries (all of them rectangular following the geometry presented in figure 1) are considered. Specifically, two different length-to-width ratios are examined for the same piezoelectric material (PZT-5A), and their respective characteristics are presented in tables 2 and 3. Specifically, the geometric data (table 2) is obtained from [5, 18, 36] for configurations A, B, and C, respectively. Note that the geometric parameters presented in table 2 are also defined explicitly in figure 1. Additionally, the electromechanical properties (table 3) are obtained from [27]. Configurations A, B, and C were carefully chosen to exemplify the procedure to propagate the uncertainties over different and well-known harvesters, i.e., harvesters that have been widely studied in the literature, experimentally tested, and modeled using the procedure presented in section 2.1. Each harvester is studied based on different scenarios, a brief description of which is presented in table 4. The first scenario corresponds to the traditional approach in which all the model parameters are treated as free of uncertainties (nominal values). The second scenario assumes typical uncertainties in model parameters (as described in previous sections). The last scenario increases the uncertainty of the length with the aim to simulate an imperfect clamping. In particular, for the latter scenario, the uncertainty of the length is increased by changing only the higher limit of the PDF associated with the length. Note that imperfect clamping only increases the length, rather than decreasing its value. These scenarios can be established for harvesters with and without tip masses (22.74, 20, and 12 g for configurations A, B, and C, respectively). Note that each configuration has a specific identifier, as listed in table 4.

Table 3. Nominal characteristic for piezoelectric material (PZT-5A) and its electro-mechanical properties.

	All configurations
ρ_p	7800 kg m^{-3}
s_{11}^E	16.4 $\times$ 10^{-12} m^2 N^{-1}
d_{31}	$-$171 $\times$ 10^{-12} C N^{-1}
ε_{33}^T	1700 $\times$ (8.854 $\times$ 10^{-12}) F m^{-1}

Table 4. Identification of the three different scenarios evaluated in the numerical analysis.

	Identifier	Uncertainties	Tip mass	Imperfect clamping
Scenario 1	*Nom*	No	No	No
	Nom-M	No	Yes	No
Scenario 2	*Unc*	Yes	No	No
	Unc-M	Yes	Yes	No
Scenario 3	*Unc-I*	Yes	No	Yes
	Unc-M-I	Yes	Yes	Yes

To propagate the uncertainties, it is assumed that each single variable is defined by an uncorrelated and uniform PDF. This PDF is bounded by the values presented in tables 5 and 6.

With all of the uncertain variables defined, it is possible to estimate the output variability, e.g., to identify the expected

Table 5. Bounds for the uniform PDF associated with the geometric parameters; bounds are expressed in terms of the nominal values.

ID	Configuration	h_p	h_s	M_t	L	b
Unc	A	±10%	±10%	—	±1%	±2%
	B	±5%	±4%	—	±1%	±2%
	C	±10%	±20%	—	±1%	±2%
Unc-M	A	±10%	±10%	±5%	±6%	±2%
	B	±5%	±4%	±5%	±6%	±2%
	C	±10%	±20%	±5%	±6%	±2%
Unc-I	A	±10%	±10%	—	−1% to 4%	±2%
	B	±5%	±4%	—	−1% to 4%	±2%
	C	±10%	±20%	—	−1% to 4%	±2%
Unc-M-I	A	±10%	±10%	±5%	−6% to 9%	±2%
	B	±5%	±4%	±5%	−6% to 9%	±2%
	C	±10%	±20%	±5%	−6% to 9%	±2%

Table 6. Bounds for the uniform PDF associated with the electromechanical parameters; bounds are expressed in terms of the nominal values, which are used for all configurations and scenarios.

Parameter	Bounds
ζ	±10%
ρ_p	±20%
ρ_s	±10%
Y_s	±10%
s_{11}^E	±20%
d_{31}	±20%
ε_{33}^T	±20%

value of the frequency response function or the confidence interval in which the actual response is expected.

4.2. Robust estimation for the frequency response function

Through the evaluation of equation (14), it is possible to obtain the expected value for the transfer function associated with the displacement, voltage, or any other important output parameter of the harvester. In particular, this work focuses on the FRF associated with the output voltage H_V. However, the results are extendable to the output current and power since these both depend on the voltage directly. A total of 10 000 samples is used with this purpose, obtaining approximation errors (equation (15)) close to 4%. Under this approach, the nominal FRF (no uncertainties taken into account) of a specific configuration (A, B, or C) could be compared with the expected value based on any of the scenarios described in table 5 (*Unc*, *Unc-I*, *Unc-M*, or *Unc-M-I*). Then, it is expected to have 10 000 different FRFs for each scenario and for each configuration, allowing the estimation of the expectation and the voltage threshold for a specific probability of exceedance.

The expected natural frequencies for each configuration under different scenarios are expressed in terms of nominal values and presented in table 7. The results suggest that the expected natural frequency is independent of the configuration (type of harvester), relying primarily on the nominal value and the scenario assumed. In particular, it is observed that the expected natural frequency obtained assuming a perfect clamping (*Unc* and *Unc-M*) corresponds to the prediction given by the nominal model. On the other hand, when an imperfect clamping is assumed (*Unc-I* and *Unc-M-I*), the nominal model overestimates the value of the natural frequency. This behavior is expected since an imperfect clamping is understood as an increment of the harvester length, where the immediate effect is a reduction in its natural frequency.

The dispersion in the natural frequency estimation is also studied. To quantify the dispersion, we identify the threshold that defines a confidence interval of 80%. Here, the thresholds for all configurations and scenarios are reported in table 8 as a percentage of their respective expected values. For example, for Configuration A under the scenario *Unc*, there is an 80% chance that the natural frequency lies in a band defined by ±9% of its expected value. In other words, the values reported in table 8 show a direct parameter to which to compare the spread of the natural frequency distribution. Here, it is important to remember that the scenario identified as *Unc* has the lowest number of associated uncertainties (table 5). The remaining three scenarios are considered with greater uncertainties associated with the harvester length in order to impose different conditions (inclusion of the tip mass and an imperfect clamping). Then, it is anticipated that for any configuration (A, B, or C), scenario *Unc* gives the lowest dispersion of the natural frequency, whereas scenario *Unc-M-I* gives the largest. It is interesting to note that the difference in the dispersion between scenarios *Unc* and *Unc-M-I* is not dramatic; it increases from ±9% to ±11% for Configuration A; from ±7% to ±11% for Configuration B; and from ±12% to ±15% for Configuration C. These results reveal that the uncertainties associated with scenario *Unc* are far more important that those associated with the location of the tip mass and the plausibility of having an imperfect clamping.

The uncertainties also have an impact on the maximum value of the FRF. To understand the importance of this impact, first it is necessary to discuss two different approaches, assuming that: (i) the excitation frequency could have

Table 7. Expected natural frequency of the harvester. Values refer to the nominal configuration.

Expected natural frequency			
Scenario	Configuration A	Configuration B	Configuration C
Unc	ω_{Nom}	ω_{Nom}	ω_{Nom}
Unc-I	$0.97\omega_{\text{Nom}}$	$0.97\omega_{\text{Nom}}$	$0.97\omega_{\text{Nom}}$
Unc-M	$\omega_{\text{Nom-}M}$	$\omega_{\text{Nom-}M}$	$\omega_{\text{Nom-}M}$
Unc-M-I	$0.97\omega_{\text{Nom-}M}$	$0.97\omega_{\text{Nom-}M}$	$0.96\omega_{\text{Nom-}M}$
Nominal values	$\omega_{\text{Nom}} = 28.5$ Hz $\omega_{\text{Nom-}M} = 14.2$ Hz	$\omega_{\text{Nom}} = 46.8$ Hz $\omega_{\text{Nom-}M} = 17.5$ Hz	$\omega_{\text{Nom}} = 114$ Hz $\omega_{\text{Nom-}M} = 44$ Hz

Table 8. Confidence interval of 80% for the natural frequency. The confidence intervals are expressed as percentages of the respective expected values.

Confidence interval			
Scenario	Configuration A	Configuration B	Configuration C
Unc	±9%	±7%	±12%
Unc-I	±10%	±8%	±13%
Unc-M	±10%	±10%	±14%
Unc-M-I	±11%	±11%	±15%

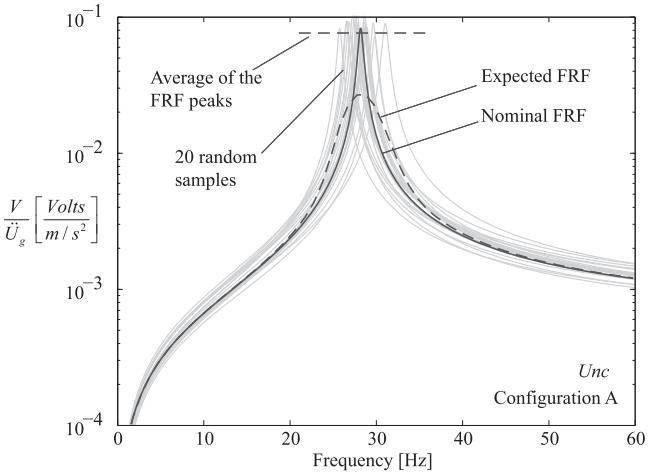

Figure 3. Typical FRF of a PEH; comparison between nominal prediction, expected value, and different realizations, assuming uncertainties in the model parameters.

any desirable value, or (ii) the excitation frequency is given. To illustrate these approaches, 20 of the 10 000 FRFs associated with Harvester A under the *Unc* configuration are chosen randomly and presented in gray in figure 3. The first approach here corresponds to the performance of the average of the FRF peaks (horizontal black dotted line in figure 3), which is close to the peak value of the nominal FRF (shown with a black solid line). However, this procedures relies on the assumption that the harvesters should be working in a resonance condition. This condition is unrealistic since in real implementation the excitation frequency is not controllable, i.e., it is not feasible to impose a desired excitation frequency. Then, the concern here is the estimation of the amplitude of FRF for a given excitation frequency. In other words, the important quantity is the average of the FRFs evaluated at the same excitation frequency (second approach); this is represented by the black dotted curve in figure 3. Ultimately, this curve corresponds to the expected FRF for Harvester A under scenario *Unc*. The peak of the expected FRF differs significantly to the nominal value; in fact the ratio of the former to the latter is 0.32. This behavior is explained since harvesters with similar natural frequencies generate significantly different responses when they are excited identically, especially when the excitation is close to the nominal natural frequency.

Table 9 presents a comparison between the nominal and the expected FRF peaks. In general, the expected FRF peak decreases with increments of the uncertainties. The larger the uncertainty in the model parameters, the greater the dispersion of the natural frequencies, which finally induces the observed decrement of the expected FRF peak in table 9. Note that this behavior depends on the dispersion of the natural frequency, rather than its expected value. Additionally, the maximum dispersion of the FRF amplitude is presented in table 10. Again, a confidence interval of 80% is used and the respective bounds are expressed as a percentage of the expected FRF. In comparison to the behavior of the natural frequency dispersion (table 8), the dispersion of the FRF amplitude is considerably larger (table 10). However, as it occurs in the natural frequencies, the dispersion of the FRF amplitude for harvesters with tip mass and imperfect clamping, are not as relevant as the dispersion associated with the harvester under the standard scenario *Unc*.

To better represent the results obtained, let us introduce a graphic representation of the FRF. For instance, the FRF of Harvester A under different scenarios is presented in figure 4. Here, the nominal FRF is represented by a black solid curve, whereas the expected FRF is expressed as a black dotted curve. Figures 4(a)–(d) corresponds to different scenarios: *Unc*, *Unc-I*, *Unc-M,* and *Unc-M-I*, respectively. The lower limit of the shaded area defines the threshold for a probability of exceedance of 90% (i.e., there is a 90% probability that the output voltage will be above this line), whereas the upper limit defines the threshold for a probability of exceedance of 10% (i.e., there is a 10% probability that the output voltage will be above this line). In other words, the shaded area

Table 9. Expected maximum response of the harvester. Values refer to the nominal configuration.

	Expected natural frequency		
Scenario	Configuration A	Configuration B	Configuration C
Unc	0.32 max $\lvert H_V \rvert_{\text{Nom}}$	0.38 max $\lvert H_V \rvert_{\text{Nom}}$	0.26 max $\lvert H_V \rvert_{\text{Nom}}$
Unc-I	0.32 max $\lvert H_V \rvert_{\text{Nom}}$	0.35 max $\lvert H_V \rvert_{\text{Nom}}$	0.25 max $\lvert H_V \rvert_{\text{Nom}}$
Unc-M	0.29 max $\lvert H_V \rvert_{\text{Nom-}M}$	0.30 max $\lvert H_V \rvert_{\text{Nom-}M}$	0.23 max $\lvert H_V \rvert_{\text{Nom}}$
Unc-M-I	0.26 max $\lvert H_V \rvert_{\text{Nom-}M}$	0.28 max $\lvert H_V \rvert_{\text{Nom-}M}$	0.22 max $\lvert H_V \rvert_{\text{Nom}}$
Nominal values	max $\lvert H_V \rvert_{\text{Nom}} = 0.08$ V s^2 m^{-1} max $\lvert H_V \rvert_{\text{Nom-}M} = 0.13$ V s^2 m^{-1}	max $\lvert H_V \rvert_{\text{Nom}} = 0.02$ V s^2 m^{-1} max $\lvert H_V \rvert_{\text{Nom}} = 0.05$ V s^2 m^{-1}	max $\lvert H_V \rvert_{\text{Nom}} = 0.02$ V s^2 m^{-1} max $\lvert H_V \rvert_{\text{Nom}} = 0.04$ V s^2 m^{-1}

Table 10. Confidence interval of 80% for the maximum response. The confidence intervals are expressed as percentages of the respective expected values.

	Confidence interval		
Scenario	Configuration A	Configuration B	Configuration C
Unc	−72% to 136%	−69% to 117%	−74% to 150%
Unc-I	−72% to 138%	−70% to 130%	−75% to 152%
Unc-M	−72% to 144%	−71% to 140%	−76% to 156%
Unc-M-I	−72% to 149%	−73% to 149%	−76% to 157%

represents a confident interval of 80%. The first interesting result is that, independent of the scenario, the probability of obtaining the nominal peak amplitude is less than 10%. This situation is revealed since the nominal peak is above the 10% probability of exceedance curve. Additionally, it is observed that the nominal FRF amplitude is greater than expected in a narrow band around the resonance, specifically in the bandwidth less than 2 Hz. On the contrary, outside this band, the nominal FRF underestimates the expected amplitude of the FRF. These results have an important implication for the design process of PEHs; more specifically, when the vibration source is a narrow band process, since there is a 90% probability that the actual output voltage is lower than the nominal value. In addition, note that the dispersion represented in the shaded area is not affected significantly by the installation of the tip mass or the assumption of an imperfect clamping. For the sake of brevity, it is decided not to present the results corresponding to Harvester B and C since they follow the same trend as the results presented in figure 4.

It is important to remember that the uncertainties used in this work correspond to the typical uncertainties reported by the harvester manufacturers (which are, in fact, large numbers); in other words, it is assumed that the user does not have the feasibility to conduct experiments to refine the information and, consequently, to improve the predictions. It is clear that is essential to reduce the uncertainties given by the manufacturers, but the question that arises is which model parameter or group of contributes significantly to the dispersion of the FRF. This topic is covered in section 4.3.

4.3. Sensitivity analysis

With all the uncertain variables defined, it is convenient to conduct a sensitivity analysis to identify the parameters with greater influence on the FRF of the harvester. In section 3.3, we discussed that the variability in the output estimation of a system could be decomposed as first- and second-order contributions. The configurations studied here contain 11 or 12 parameters, depending on whether the tip mass is considered. As a result, the variability associated with the FRF is decomposed in 11 indices of first order together with 55 indices of second order for configurations without tip mass (66 different Sobol indices); and 12 indices of first order and 66 indices of second order for configurations with tip mass (78 different Sobol indices). The Sobol index could be understood as the perceptual contribution of a specific parameter or a combination of parameters in the variability of the FRF. In other words, the sum of all Sobol indices should be equal to 1 (or 100%). In this study, only the first and second order indices are computed. Note that there are 66 or 78 different indices depending on whether the tip mass is installed, meaning that on average, the value of each index should be 0.0152 (1.52%) or 0.0128 (1.28%), respectively. For the sake of simplicity, only indices with values greater than three times the average are considered important, i.e., 0.04 and 0.045 for configurations with and without tip mass, respectively.

The Sobol indices are obtained by solving equation (21) through Monte Carlo simulations, employing 30 000 samples, and imposing a maximum c.o.v equal to 5%. The first- and second-order indices are identified for different excitation frequencies bounded between ±10% of the fundamental frequency of the harvester.

The most relevant indices for configurations A, B, and C are presented in figures 5–7, respectively. In particular, figure 5 shows the Sobol indices for Harvester A under the scenarios *Unc* and *Unc-M-I*. For the scenario *Unc*, it is observed that the variance of the output voltage is driven primarily by four parameters: s_{11}, h_s, h_p, and ρ_p. These parameters are responsible for up to 40% of the FRF variance for frequencies close to the resonance. Additionally, it is observed that the impact of these parameters in the FRF variance decreases significantly at resonance, indicating that the rest of the parameters involved in the dynamic of the harvester acquire more importance. Nevertheless, the four parameters mentioned, or a combination of them, still impact the total variance of the FRF at a minimum of 20%. On the other hand, the scenario *Unc-M-I* is driven predominantly by L and s_{11}, which is expected since the major difference

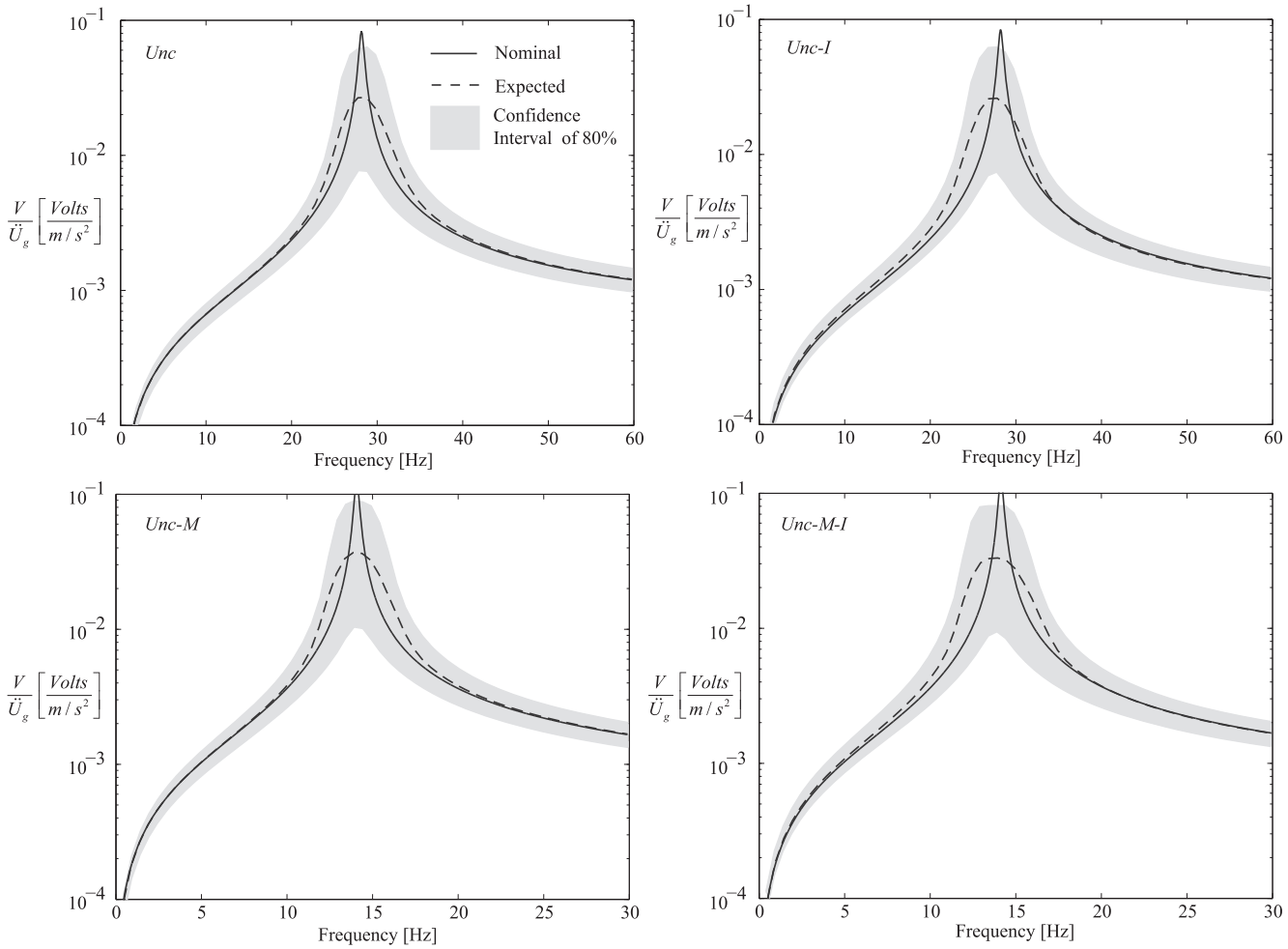

Figure 4. Frequency response function associated with the output voltage of a PEH (Configuration A) excited with different acceleration frequencies close to the first resonance. The first natural frequency is 28.5 Hz for *Unc* and *Unc-I*, and 14.2 Hz for *Unc-M* and *Unc-M-I*.

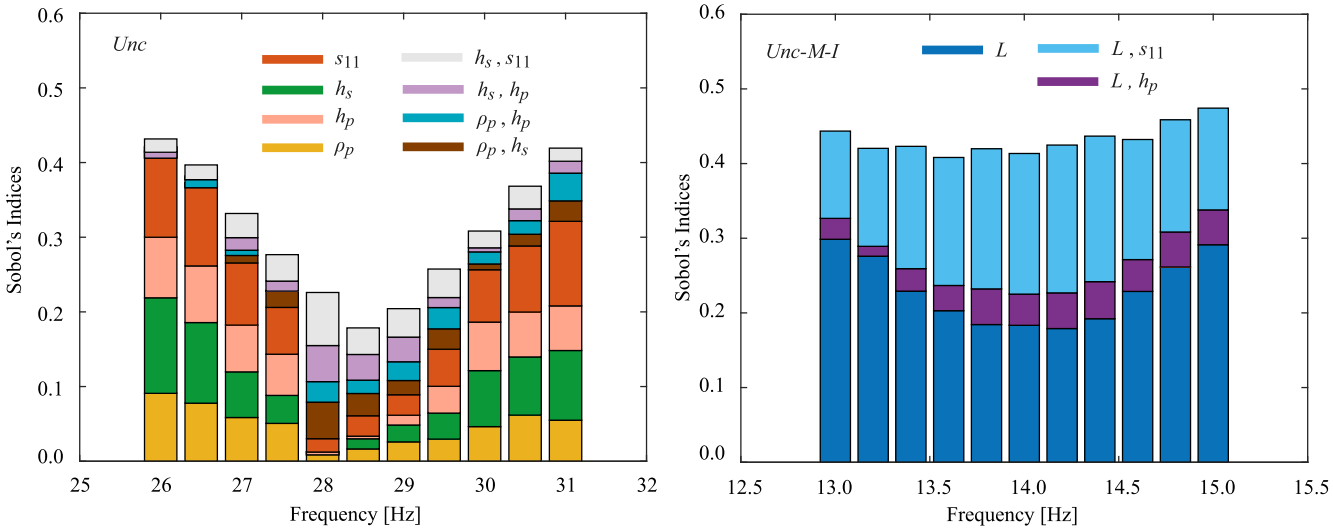

Figure 5. Sobol indices associated with the output voltage of a PEH (Configuration A) excited with different acceleration frequencies close to the first resonance. The first natural frequency is 28.5 Hz *Unc* and 14.2 Hz for *Unc-M-I*.

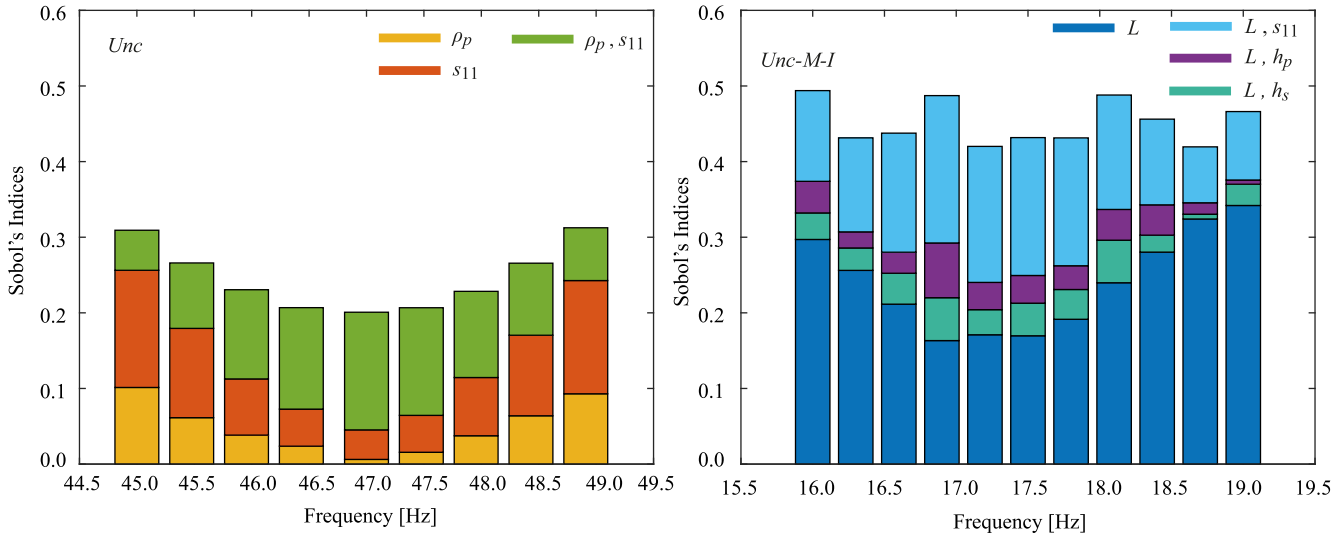

Figure 6. Sobol indices associated with the output voltage of a PEH (Configuration B) excited with different acceleration frequencies close to the first resonance. The first natural frequency is 46.8 Hz for *Unc* and 17.5 Hz for *Unc-M-I*.

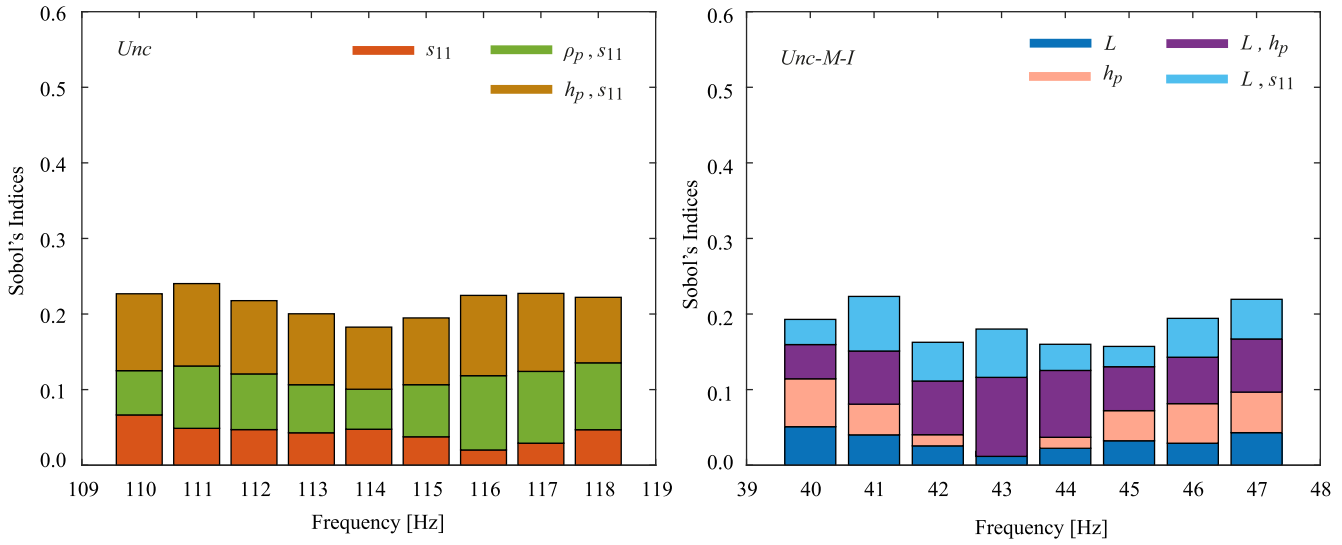

Figure 7. Sobol indices associated with the output voltage of a PEH (Configuration C) excited with different acceleration frequencies close to the first resonance. The first natural frequency is 114 Hz for *Unc* and 44 Hz for *Unc-M-I*.

between the scenarios is the uncertainty assigned to L (as was discussed previously). For this case, the contribution of L and s_{11} is close to the 35% of the total variance of the FRF for any frequency studied.

In configuration B (figure 6), the parameters s_{11} and ρ_p contribute to 20% of the FRF variance for the *Unc* scenario; while the parameters L and s_{11} contribute to 35% of the FRF variance for scenario *Unc-M-I*. For configuration C (figure 7), the greatest contribution to the FRF variance (20%) for the *Unc* scenario is attributed to three parameters: s_{11}, h_p, and ρ_p. On the other hand, the variance in scenario *Unc-M-I* is driven by L, s_{11}, and h_p. Ultimately, regardless the configuration of the harvester, we can conclude that the most important parameters for the estimation of the FRF are: s_{11}, h_p, and ρ_p for the scenarios *Unc* and L, $s_{11,}$ and h_p for the scenario *Unc-M-I*. In other words, if the uncertainty associated with s_{11}, h_p, ρ_p, and L is removed, then the FRF variance is decreased by at least 20%, independent of the harvester configuration and the scenario established.

To show the impact of s_{11}, h_p, ρ_p, and L in the FRF variance, we compared the expected FRF and the confidence interval of 80% with and without assumed uncertainties in s_{11}, h_p, ρ_p, and L. In particular, figure 8 shows the referred comparison for Configuration A under the *Unc* scenario. The left figure shows the nominal FRF with its corresponding expected value. Red is assigned to the configuration where s_{11}, h_p, ρ_p, and L are free of uncertainties, whereas gray corresponds to the case presented in figure 4. Here, the advantage of controlling the uncertainties in the referred parameters is evident since the expected curve closely

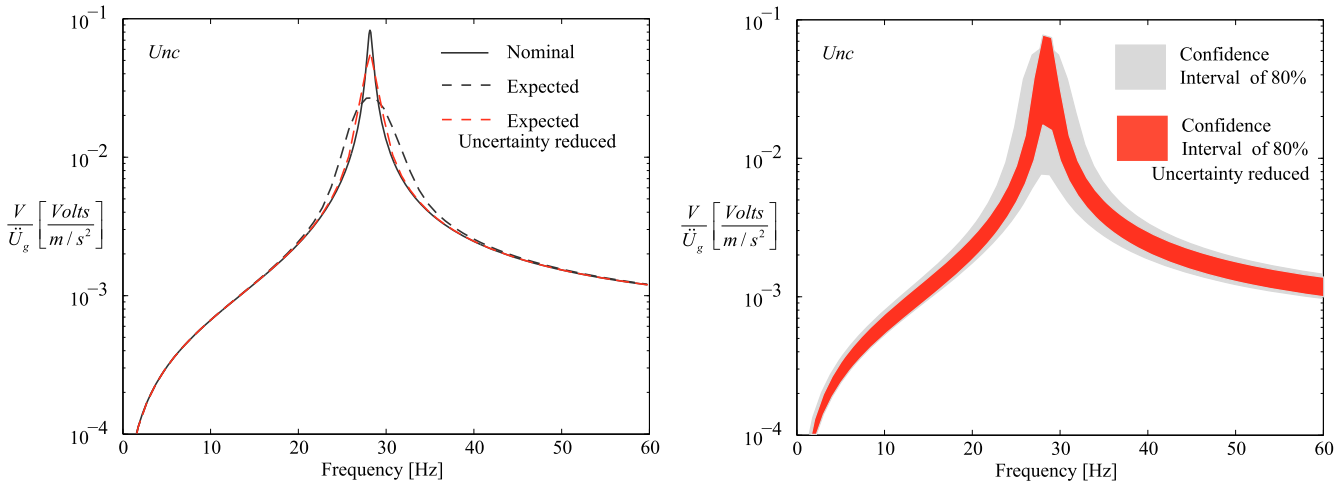

Figure 8. Nominal FRF and its interval confidence (80%) assuming uncertainties and no uncertainties in the piezoelectric elastic modulus, density, and thickness.

approximates the nominal one. The figure on the right presents a visualization of the FRF variance reduction.

5. Conclusions

A robust framework to propagate uncertainties in PEHs is presented. The framework presents a series of significant advantages: (1) it is compatible with any well-known energy harvester performance predictor (deterministic models), (2) it is independent of the number of piezoelectric and substructure layers, and (3) it allows us to define expected values and confidence intervals for the FRF associated with the output voltage.

An extensive literature review was conducted to identify the common uncertainties related to the geometric and electromechanical properties of PEHs. For the most common commercial piezoelectric harvesters, the properties of the piezoelectric material exhibit the greatest variances compared to that of the remaining parameters (close to 20% of their nominal values).

For the configuration studied, the fundamental frequency of the harvester can vary by approximately $\pm 10\%$ of the nominal value. Important differences between the expected and nominal peak of the FRF were identified, revealing that the probability of obtaining the nominal peak amplitude is less than 10%. In addition, a global variance-based sensitivity analysis was implemented. The highest sensitivities on the FRF were identified as the piezoelectric layer thickness, its elastic modulus, and its density. The contribution of these three parameters to the output voltage variability lies between 20% and 40%. Although the reliability of the framework was demonstrated by the proper use of the model predictor and the Monte Carlo method, it is also important to conduct an extensive experimental test (which is proposed as a future work) to propose a general method to update the uncertainties and compare them with the predictions.

In general, the results obtained endorse the need to quantify and propagate the uncertainties in PEHs. In this sense, the framework presented constitutes a powerful tool in the robust design and prediction of PEH performance.

Acknowledgments

This research is supported by the Comision Nacional de Investigacion Cientifica y Tecnologica de Chile through the project CONICYT/FONDECYT/3160491.

References

[1] Erturk A and Inman D J 2011 *Piezoelectric Energy Harvesting* (New York: Wiley)
[2] Lei A *et al* 2011 MEMS-based thick film PZT vibrational energy harvester *2011 IEEE 24th int. conf. on Micro electro mechanical systems (MEMS)* pp 125–8
[3] Roundy S, Wright P K and Rabaey J 2003 A study of low level vibrations as a power source for wireless sensor nodes *Comput. Commun.* **26** 1131–44
[4] DuToit N E, Wardle B L and Kim S 2005 Design considerations for mems-scale piezoelectric mechanical vibration energy harvesters *J. Integr. Ferroelectr.* **71** 121–60
[5] Erturk A and Inman D J 2008 A distributed parameter electromechanical model for cantilevered piezoelectric energy harvesters *Trans. ASME. J. Vib. Acoust.* **130** 041002
[6] Sodano H A, Park G and Inman D J 2004 Estimation of electric charge output for piezoelectric energy harvesting *Strain* **40** 49–58
[7] Junior C D M, Erturk A and Inman D J 2009 An electromechanical finite element model for piezoelectric energy harvester plates *J. Sound Vib.* **327** 9–25
[8] Erturk A and Inman D J 2008 On mechanical modeling of cantilevered piezoelectric vibration energy harvesters *J. Intell. Mater. Syst. Struct.* **19** 1311–25
[9] Meruane V and Pichara K 2015 A broadband vibration-based energy harvester using an array of piezoelectric beams connected by springs *Shock Vib.* **2016** 9614842
[10] Bibo A and Daqaq M F 2013 Energy harvesting under combined aerodynamic and base excitations *J. Sound Vib.* **332** 5086–102
[11] Abdelkefi A, Hajj M R and Nayfeh A H 2012 Sensitivity analysis of piezoaeroelastic energy harvesters *J. Intell. Mater. Syst. Struct.* **23** 1523–31
[12] Zhu D, Beeby S, Tudor J, White N and Harris N 2010 A novel miniature wind generator for wireless sensing applications *9th IEEE Sensors Conf., SENSORS 2010 (1–4 November 2010)* pp 1415–8

[13] Abdelkefi A, Hajj M R and Nayfeh A H 2013 Piezoelectric energy harvesting from transverse galloping of bluff bodies *Smart Mater. Struct.* **22** 015014
[14] Lin H C, Wu P H, Lien I C and Shu Y C 2013 Analysis of an array of piezoelectric energy harvesters connected in series *Smart Mater. Struct.* **22** 094026
[15] Szarka G D, Stark B H and Burrow S G 2012 Review of power conditioning for kinetic energy harvesting systems *IEEE Trans. Power Electron.* **27** 803–15
[16] Scruggs J T 2010 On the causal power generation limit for a vibratory energy harvester in broadband stochastic response *J. Intell. Mater. Syst. Struct.* **21** 1249–62
[17] Ali S F, Friswell M I and Adhikari S 2010 Piezoelectric energy harvesting with parametric uncertainty *Smart Mater. Struct.* **19** 105010
[18] Erturk A and Inman D J 2009 An experimentally validated bimorph cantilever model for piezoelectric energy harvesting from base excitations *Smart Mater. Struct.* **18** 025009
[19] Steiner & Martins, INC 2016 https://steminc.com
[20] Morgan Advanced Materials 2016 http://morgantechnicalceramics.com/
[21] APC International, Ltd 2016 https://americanpiezo.com
[22] Goldschmidtboeing F and Woias P 2008 Characterization of different beam shapes for piezoelectric energy harvesting *J. Micromech. Microeng.* **18** 104013
[23] Jeon Y B, Sood R, Jeong J-H and Kim S-G 2005 MEMS power generator with transverse mode thin film PZT *Sensors Actuators* **122** 16–22
[24] Levy M, Bass H E, Stern R R and Keppens V 2001 *Handbook of Elastic Properties of Solids, Liquids, and Gases* (New York: Academic)
[25] Hess P E, Bruchman D, Assakkaf I A and Ayyub B M 2002 Uncertainties in material and geometric strength and load variables *Naval Eng. J.* **114** 139–66
[26] Ashby M 2011 *Material Selection in Mechanical Design* 4th edn (Amsterdam: Elsevier)
[27] efunda 2016 http://efunda.com/
[28] Kim J E and Kim Y Y 2011 Analysis of piezoelectric energy harvesters of a moderate aspect ratio with a distributed tip mass *J. Vib. Acoust.* **133** 041010
[29] Sinocera 2016 http://sinocera.net/
[30] Beck J L and Taflanidis A A 2013 Prior and posterior robust stochastic predictions for dynamical systems using probability logic *Int. J. Uncertain. Quantif.* **3** 271–88
[31] Lutes L D 1997 *Stochastic Analisys of Structural and Mechanical Vibrations* (Englewood Cliffs, NJ: Prentice-Hall)
[32] Sobol I M 1993 Sensitivity estimates for nonlinear mathematical models *Math. Model. Comput. Exp.* **1** 407–14
[33] Sobol I M 2001 Global sensitivity indices for nonlinear mathematical models and their Monte Carlo estimates *Math. Comput. Simul.* **55** 271–80
[34] Zhang X and Pandey M D 2014 An effective approximation for variance-based global sensitivity analysis *Reliab. Eng. Syst. Saf.* **121** 164–74
[35] Jia G and Taflanidis A A 2016 Efficient evaluation of sobol'indices utilizing samples from an auxiliary probability density function *J. Eng. Mech.* **142** 04016012
[36] Ting Y, Hariyanto G, Hou B K and Huang C Y 2009 Evaluation of energy harvesting by using piezoelectric unimorph ceramics *Int. Conf. on Information and Automation 2009, ICIA'09* pp 778–83